Estimation of stress in specimens loaded with ultrasonic fatigue machines

Vincent Jacquemain, Nicolas Ranc, C. Cheuleu, Vincent Michel, Véronique Favier, Olivier Castelnau, D. Vinci, D. Thiaudiere, C. Mocuta

Estimation of stress in specimens loaded with ultrasonic fatigue machines

V. Jacquemain [a,*], N. Ranc [a], C. Cheuleu [a], V. Michel [a], V. Favier [a], O. Castelnau [a], D. Vinci [a], D. Thiaudiere [b], C. Mocuta [b]

[a] PIMM, Arts et Metiers Institute of Technology, CNRS, Cnam, HESAM University, 151 Boulevard de l'Hopital, Paris, France
[b] Synchrotron SOLEIL, L'Orme des Merisiers Saint-Aubin BP 48, 91192 Gif-sur-Yvette, France

ARTICLE INFO

Keywords:
Very High Cycle Fatigue
Ultrasonic fatigue machine
Stress amplitude analysis
Time-resolved X-ray diffraction

ABSTRACT

Piezo-electric ultrasonic fatigue machines are used to carry out fatigue tests more rapidly than what is possible using other technologies, at a frequency of 20 kHz. The very high cycle fatigue (VHCF) domain can be studied with these machines as 10^9 cycles are reached within 14 h when specimens are loaded at stress amplitudes below the yield stress or conventional fatigue strength. The estimation of stress in specimens fatigued at high frequency is a current challenge when adopting this technology. This paper discusses the accuracy and reliability of three methods used to estimate stress amplitudes in specimens subjected to VHCF tests at a high loading frequency. Two historically used methods using strain gauges and a laser vibrometer are discussed and compared with a third, recently developed method based on time-resolved in situ X-ray diffraction (XRD). The three methods are applied to estimate the stress amplitude in a pearlitic steel specimen. The experimental artifacts and uncertainties are evaluated quantitatively to compare the benefits and limits of the methods. The experimental results show that the three methods correctly estimate the stress amplitudes applied to fatigued specimens.

1. Introduction

Several industrial applications, especially in transportation and energy production have shown fatigue failure in the Very High Cycle Fatigue (VHCF) domain. For such lifetimes, it takes too long to determine the S-N curve experimentally with conventional hydraulic fatigue machines, operating typically at a frequency of $\sim$ 10 Hz. As an example, at 10 Hz, it takes three years of testing to reach 10^9 cycles for a single specimen. Efforts made to develop fatigue machines that load specimens to reach a very high number of cycles more rapidly and to study damage mechanisms taking place in the VHCF regime were described in [1–3].

For several decades, studies have focused on improving the control of piezo-electric converters, in the development of ultrasonic fatigue machines. This type of piezo-electric machine was initially proposed in the 1950s by Mason [4]. The machine loads a specimen (itself considered as a mass-spring system) by vibrating it in its first longitudinal mode. Such technology is designed to reach a vibration frequency close to 20 kHz [5,6] and up to 30 kHz [7] depending on the setup. The vibration is thus a perfect tension–compression loading with a stress ratio $R = -1$. Owing to the very high frequency, this type of machine reaches 10^9 cycles within only 14 h and allows the investigation of the VHCF domain.

One issue to be addressed when using a fatigue machine at 20 kHz is the rise in the specimen temperature when applying high loading amplitudes. Two solutions have been proposed to limit the temperature increase (to a maximum of 10 °C). (i) Bathias and coworkers [8,9] proposed blowing cold pulsed air on a specimen during continuous loading. (ii) S. Stanzl-Tschegg and coworkers [2,10] suggested a second technological solution, "pulse-pause mode", in which machines operate in blocks of a given number of cycles followed by pauses to give time for heat to dissipate during the test. During pulse-pause loading, the specimen can also be cooled by cold pulsed air. The pulse-pause technology is more efficient in reducing the specimen heating. Sun et al. [11] measured increases in the temperature of GCr15 steel loaded at 850 MPa of 70 °C in continuous mode and only 50 °C in pulse-pause mode. The target loading amplitude is generally reached in less than 2000 cycles ($\sim$ 0.1 s) only at the beginning of a test in the case of Bathias' machines and after 100 cycles ($\sim$ 0.005 s) for each block in the case of Stanzl-Tschegg's machines. Typically, the loading block duration ranges between 50 and 250 ms, and the pause block duration varies from 250 to 2500 ms. The history effect of these successive short loading phases has been found to artificially extend fatigue life [11].

The second difficulty when using a fatigue machine at 20 kHz is the precise estimation of the stress amplitudes applied to the specimen

during the test. This estimation is vital for following the applied load during the test. A control loop of a fatigue test relies on the accuracy of stress estimation. The stress level is the standard quantity used to compare fatigue loadings at different frequencies and to compare tests conducted using different technologies, such as the comparison of bending or torsion with classical push–pull loading [7,12]. Additionally, fatigue criteria such as those of Crossland and Dang-Vang [13,14] are usually expressed in terms of stresses. Therefore, being able to estimate stress amplitudes during fatigue tests is fundamental. According to the type of test conducted, fatigue machines are strain- or stress-controlled. Low Cycle Fatigue (LCF) tests are commonly total strain-controlled because macroscopic plastic strain might occur. High Cycle Fatigue (HCF) tests are commonly stress controlled. In the case of VHCF tests using ultrasonic fatigue machines, the stress (and strain) levels are so low that it is equivalent to conduct stress-controlled or strain-controlled tests. Such machines are controlled with a piezo-electric converter on which a precise electrical voltage is supplied [15]. Through a calibration, the supplied voltage is equivalent to a certain displacement amplitude at the end of the machine. This statement is only strictly true when no damage or macro-plastic deformation forms in the specimen or when the specimen geometry does not change with a temperature increase in its central part. One difficulty in adopting ultrasonic fatigue machines is the estimation of the applied stress when only precise information on the prescribed displacement amplitude is available. Thus, the stress has to be estimated from complementary measurements. Very few papers in the literature and no standard provide a consensus on how the stress estimation can be achieved during ultrasonic fatigue tests.

Three methods of estimating the stress amplitude have been reported in the literature:

- The first method involves gluing strain gauges to the specimen to measure the uniaxial total strain (that is $\Delta L/L_0$). The specimen is loaded at low stress and is supposed to deform in a purely elastic manner, i.e., the plastic contribution is neglected. The stress is then obtained by multiplying the total strain by the isentropic elastic modulus. A complete description of the state-of-the-art can be found in [10,16,17].
- The second method uses a laser vibrometer to measure the displacement at the free end of the ultrasonic machine. The stress field within the specimen can then be estimated by computing the response of a modeled specimen with a 1D or 3D geometry loaded in push–pull mode, and assuming that the specimen behavior is purely elastic [9,10,16].
- More recently, Ors et al. [18] developed a third method based on measurements of the elastic strain. The method requires that time-resolved X-ray diffraction (XRD) be carried out in situ at the loading frequency (20 kHz) on a synchrotron beamline. This method is the first in situ time-resolved XRD application at VHCF and was also recently developed independently by Fitzka et al. in [19] who investigated phase transformation in Nitinol. Complementary studies that used x-rays at VHCF essentially focused on ex-situ tomography measurements allowing the analysis of the damage network [16,20].

This paper makes a comprehensive comparison of the three methods of estimating stress amplitudes in a fatigue test conducted at 20 kHz. The accuracy and capacity of the methods in estimating stress heterogeneities are discussed. This requires first an in-depth analysis of the causes of experimental uncertainties in an ultrasonic fatigue test. Therefore, Section 2 presents the ultrasonic fatigue machine technology and explain the design of fatigue specimens. Section 3 will present the three methods used to estimate stress amplitudes in ultrasonic fatigue tests at 20 kHz. Finally, in Section 4, experimental results obtained for pearlitic steel (as a study case) are presented and the reliability and capability of the three methods are discussed.

2. Experimental setup

2.1. Setup of the ultrasonic fatigue machine

The present study used an ultrasonic fatigue machine to load specimens at 20 kHz. This machine is based on the original design of Bathias and coworkers [8], see Fig. 1. The machine comprises a power generator, a piezo-electric converter from Branson^{TM} (referenced as 2000 Series Model CR-20), which converts an electrical signal into mechanical vibrations, a booster, and a horn that amplifies the displacement by a factor of 2.6. The converter is continuously refreshed with a cold air flux such that its temperature is constant. The specimen is screwed at the free end of the horn but, in this section, we first characterize the behavior of the machine itself with no specimen attached to it. Having a specimen screwed at the end of the horn slightly modifies the harmonic response of the system, which is characterized, in Section 2.2. The input of the converter is the voltage $u(t)$ supplied by the generator. The current $i(t)$ and displacement amplitude of the end of the horn $d(t)$ are the two outputs. Therefore, the electrical transfer function of the piezo-electric system is obtained, in the case of harmonic loading using the complex notations, as

$$H(j\omega) = \frac{I(\omega)}{U(\omega)}, \tag{1}$$

with ω the angular frequency and $I(\omega)$ and $U(\omega)$ the complex amplitudes of the current and the voltage. The gain $G(\omega)$ of the system is defined as the modulus of the transfer function and computed as $|H(j\omega)|$. The phase φ of the system is defined as the argument of the transfer function $\varphi = Arg(H(j\omega))$. Fig. 2a plots the measured gain $G(\omega)$ (in dB) of the transfer function against the frequency for a sinusoidal input voltage of amplitude 15 V. This curve has two extrema: a maximum (4 dB) at a frequency of 20090 Hz and a minimum (-65 dB) at 20232 Hz. These frequencies are respectively referred to as the resonance and anti-resonance of the system [1]. At this anti-resonance frequency, the system needs the smallest amount of average power to work. The provided power compensates for the energy dissipated by the system. The system was thus made to work at its anti-resonance frequency.

The displacement amplitude at the free end of the horn was measured using a HSV 2001 laser vibrometer and is plotted in Fig. 2b against the frequency for a voltage amplitude of 15 V. As the frequency approaches the resonance, a larger displacement amplitude is provided but more current is used to obtain this displacement. There are thus two benefits of working at a frequency close to the anti-resonance frequency, namely less power required for operation and a displacement amplitude that is less sensitive to frequency shifts (which is a property that is useful in carrying out mechanical tests under precisely controlled conditions), even though a lower displacement amplitude is accessible at (0.25 µm at 20232 Hz for a voltage amplitude of 15 V). The phase φ between the current and voltage supplied to the system is plotted against the frequency, for a voltage amplitude of 15 V in Fig. 2c. Sharp evolutions are close to the resonance and anti-resonance frequencies [2].

The remote control of the machine is needed to ensure that the machine works continuously at a frequency close to the anti-resonance frequency of the system. To this end, the phase plays an important role in controlling the machine because the anti-resonance is characterized by a strong phase change as shown in Fig. 2c. The target phase value is 0 degree corresponding to a working frequency of 20232 Hz. During a frequency sweeping (from 20500 to 19500 Hz) at a low input

[1] These values correspond to the 'converter + booster + horn' assembly used for the present experiments

[2] It appears that in low damping systems such as the ultrasonic fatigue machine, the gain anti-resonance frequency is close to the phase anti-resonance frequency (less than 2 Hz)

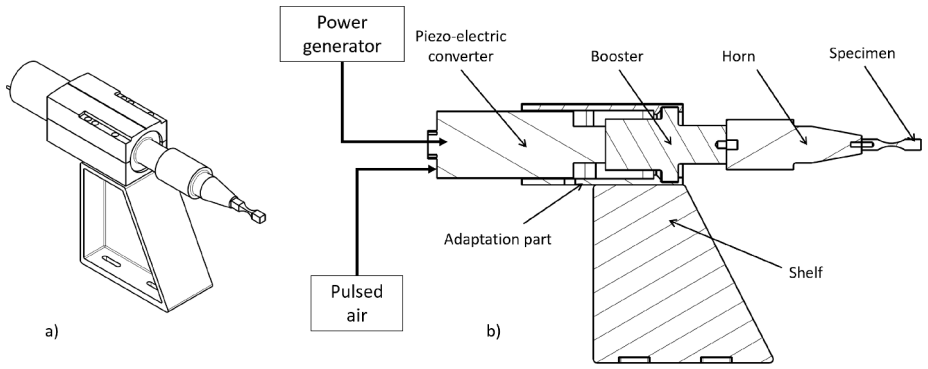

Fig. 1. Schematic representation of the ultrasonic fatigue machine - a) perspective view, b) planar view.

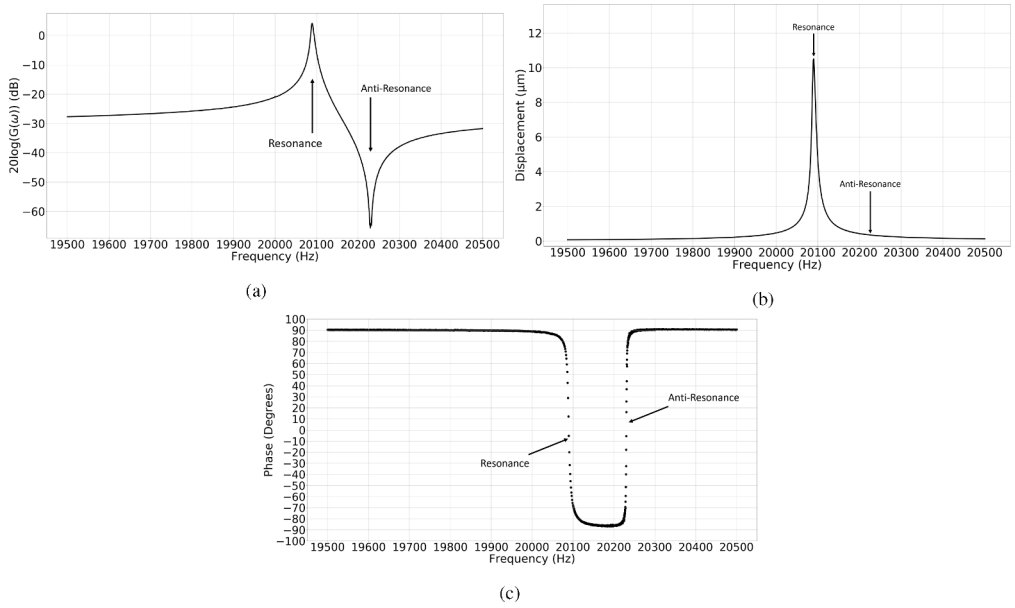

Fig. 2. Harmonic response of the ultrasonic fatigue machine obtained experimentally for a voltage amplitude of 15 V, a) gain and b) displacement and c) phase plotted with respect to the frequency. Data were acquired with a 0.5 Hz step. These measurements are for the machine with no specimen attached to it.

voltage amplitude, the frequency corresponding to the phase being 0 degree is identified and stored. Then, using a phase locked loop, the control system adjusts the frequency so that the phase remains at $\varphi = 0°$. When the anti-resonance frequency is reached, the system increases the input voltage until the expected voltage is reached. This process takes 100 ms to complete in general.

The displacement amplitude at the edge of the horn, which is measured with respect to the voltage amplitude supplied to the system without a specimen, is shown in Fig. 3. On this calibration curve, each data point is the mean value of 16 independent measurements. The input voltage amplitude ranges from 145 to 355 V, in 10 steps. Note that the working range of the converter expressed in voltage amplitude is between 10 and 1000 V. The displacement evolves linearly with the applied voltage. The standard deviation is, on average, approximately 1% of the measured displacement value, i.e. is too small to be represented on Fig. 3. This error is considered as the random error of these measurements. The systematic error due to the measurement uncertainty of the laser vibrometer affects the slope. This slope is obtained as $K_d = 0.0235\ \mu\text{mV}^{-1}$ with a systematic error of 1.2%. This curve can therefore be used for the calibration between displacement and voltage.

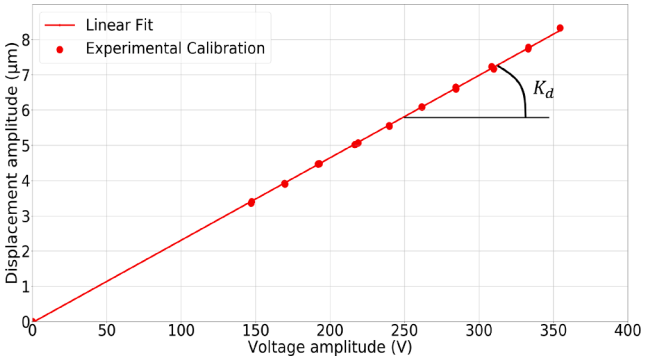

Fig. 3. Evolution of the measured displacement at the free end of the horn with respect to the applied voltage for the ultrasonic machine at the anti-resonance frequency. Each data point has been measured 16 times. The standard deviation for each point is in the order of 0.04 μm. The linear fit of the data is also shown.

2.2. Specimen design

Having characterized the machine response, the next step is to design the specimen so that the machine and specimen vibrate independently in their own vibration mode. This guarantees the decoupling of the machine and specimen; in other words, there is no stress at the interface of the horn and specimen. Thus, the specimen must vibrate in its first longitudinal mode of free vibration at a frequency close to the anti-

resonance frequency of the machine [3,21–25]. The objective of the design is therefore to determine all specimen dimensions. We consider here as a study case a specimen made of pearlitic steel (C70 steel). The specimen has the composition given in Table 1, an yield stress of 396 MPa, a fatigue strength at 10^6 cycles of 265 MPa and a fatigue strength at 10^9 cycles of 250 MPa [26].

The specimen has an hourglass shape such that stresses are concentrated at the center of the specimen to reach higher stress amplitudes. Fig. 4 shows the general geometry of specimens with rectangular cross-section designed in this study. A rectangular cross-section is necessary to conduct X-ray diffraction tests on the largest surface. Several dimensions of the specimen are fixed, especially the cross-section and the length of the central part of the specimen. Only the shaft length L_s is changed to obtain a specimen that vibrates at the desired frequency.

The density of the material was measured by double weighing. The longitudinal elastic modulus, here referred to as the isentropic modulus E_{is} and Poisson ratio ν are measured using ultrasound waves propagation method with a frequency of 5 MHz[3]. Values and uncertainties of material properties are presented in Table 2 for the pearlitic steel considered here. The uncertainties of these quantities are considered as systematic errors owing to the method used to estimate the quantities.

A 1D numerical model is used [27]. It takes into account the variation of the cross-section area along the specimen length. This model allows the rapid determination of a pre-optimized shaft length $L_s^{[1D]}$ at which the specimen vibrates in its first mode at the anti-resonance frequency of the piezo-electric system. L_s values ranging from 16 to 19 mm were tested and a value of $L_s^{1D} = 17.6$ mm was found to be optimal using this 1D model. This value is used as an initial guess in the 3D modeling. Afterward, a 3D modal analysis is necessary to consider the stress heterogeneities in the cross-section of the specimen which can affect the vibration frequency. The 3D modal simulations of the specimen are conducted using the commercial Finite Element Method (FEM) software Abaqus. The threaded hole of the specimen is not considered in the simulations because it is completely filled with a screw when the specimen is fixed to the machine. The initial guess of L_s coming from the 1D simulation greatly reduces the cost of the 3D calculation. As a matter of fact, to get a frequency of 20232 Hz, $L_s^{3D} = 17.5$ mm was determined for the 3D model [4]. This value is taken as the optimal L_s in the following.

2.3. Estimation of tolerance interval for sample dimensions and material properties

The sensitivity of geometrical parameters (S_s, S_c, L_c and L_s) and material parameters (E_{is} and ρ) on the first mode frequency of the system was investigated using the 3D FE modelling previously defined. The first derivative of the frequency with respect to parameters $\partial f/\partial P$(with P being one of the parameters mentioned above) is estimated numerically at 20232 Hz. As an example we consider the cross-sectional area S_c whose nominal value is 15 mm^2. The effect of the variation in S_c in the range of 13 −17 mm^2 on the first mode frequency is shown in Fig. 5. The frequency evolution can be approximated by a quadratic fit. The slope at 20232 Hz is:

$$\left.\frac{\partial f}{\partial S_c}\right|_{f=20232\ \mathrm{Hz}} = 468\ \mathrm{Hz\ mm^{-2}}. \tag{2}$$

The same analysis was applied to other parameters namely the dimensions and material properties. The results are given in Table 3. Note that Poisson ratio sensitivity is two orders of magnitude lower than the other parameter sensitivity. That is why it is not considered in the following.

The uncertainty of 4 GPa in the Isentropic Modulus E_{is} (see Table 2) induces an appreciable uncertainty in the estimated eigen-frequency of the first longitudinal mode of the specimen which is approximately ± 210 Hz (see Table 3) and and the highest induced uncertainty arising from material parameters. In the following, we consider that this uncertainty is the restricting criterion in terms of the possible eigen-frequency discrepancies of specimens. To ensure that no geometrical parameter overcomes the above statement criterion, specific tolerance intervals (TIs) are considered for all specimen dimensions (see Table 4).

One then verifies:

$$\Delta f = TI_P \times \frac{df}{dP} \leqslant 210\ \mathrm{Hz}. \tag{3}$$

Table 4 shows that TI of S_c is found to be on the order of ±0.45 mm^2, inducing an uncertainty of ±0.06 mm in each lateral dimension of the cross-section. TI of S_s is found to be ±2.8 mm^2 inducing an uncertainty of ±0.11 mm on each lateral dimension. Therefore, the accuracy of the cross-sectionnal dimensions must be greater than that of the lengths. A TI of ±0.4 mm and ±0.3 mm is then sufficient for L_s and L_c respectively. Following the presented procedure, the specimen dimensions and their tolerances are presented in Fig. 6. When machining, we take smaller IT than those prescribed to respect the design criterion.

2.4. Experimental validation

In addition to the experimental study carried out on the machine alone (Section 1), a similar study was carried out on the complete machine + specimen system. A first prototype specimen was machined with dimensions $L_s = 17.52$ mm, $L_c = 15.0$ mm, $S_s = 145.0$ mm^2 and $S_c = 15.06$ mm^2. Once screwed to the amplifying horn of the machine, the anti-resonance frequency detected experimentally for the complete system was found equal to 20279 Hz. This value is higher than the functionning frequency (20232 Hz) of the machine alone of + 47 Hz. An eigen-frequency of the specimen that is different from the anti-resonance frequency of the machine thus induces a shift (in this case, a shift of + 47 Hz) in the anti-resonance frequency of the complete system.

During this preliminary test, the displacement was measured at the free end of the specimen and at the horn surface (where the displacement is identical that at the top surface of the specimen). For a voltage amplitude of 215 V applied to the machine, a displacement amplitude of 4.9 μm was measured at the horn end and a displacement amplitude of 5.1μm was measured at the free end of the specimen. The displacement of the machine (without a specimen) at this voltage amplitude was 5.0μm. A 2% discrepancy in the displacement amplitude was found when a specimen was placed on the machine. Moreover, a +4% higher value at the free end of the specimen compared with the top was found, leading to a slight asymmetry of the displacement amplitude. However there is no temporal asymmetry as the loading ratio remains $R = -1$. This spatial asymmetry is induced by the operating of the complete system at a frequency that is shifted (by + 47Hz) from the nominal anti-resonance frequency of the machine without a specimen. The errors induced by dimensionnal discrepancies on the specimen are smaller than the 210Hz criterion fixed earlier. This validates the design procedure. More importantly, it is the parameter E_{is} that shows the highest influence on the frequency of the system machine + specimen compared to the machine alone.

[3] used here as the present study is based on ultrasonic fatigue (i.e., dynamic) tests that are considered adiabatic because of the very short loading period (50 μs). A small discrepancy is observed between the isentropic and isothermal modulii. These modulii are related by the following formula $E_{is} = 1/(1/E_T - T_0\alpha^2/\rho C)$, where C is the volumetric heat capacity, T_0 the ambient temperature, and α the thermal expansion coefficient.

[4] The mesh of the FE simulation was refined until a convergence was achieved with a relative error in frequency smaller than 0.01%, corresponding here to ±2 Hz and elements size of 0.4 mm

Table 1
Chemical composition of the C70 steel studied (% weight).

C	Si	Mn	S	P	Ni	Cr	Mo	Cu	Al	Sn	Fe
0.68	0.192	0.846	0.01	0.01	0.114	0.16	0.027	0.205	0.042	0.016	balance

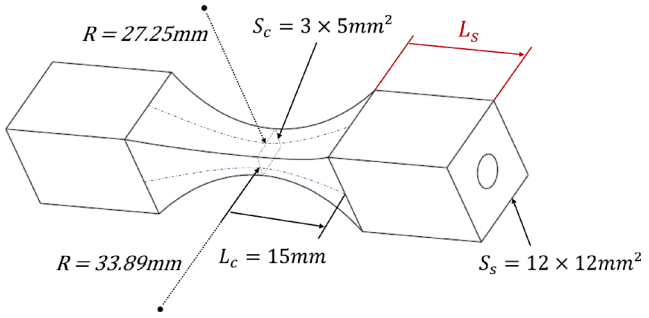

Fig. 4. Specimen geometry (dimensions provided are those that are fixed in advance. L_s is to be determined).

Table 2
Values and uncertainties on the properties of pearlitic steel studied.

Parameters	Reference value	Uncertainty
ρ (kgm^{-3})	7800	±140
c (ms^{-1})	5115	±100
E_{is} (GPa)	204	±4

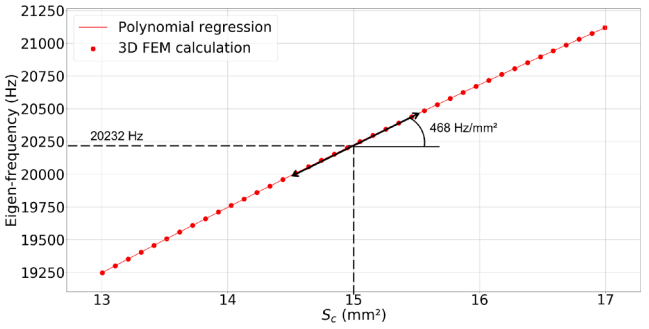

Fig. 5. Evolution of the specimen eigen-frequency with the cross-section size at the center of the specimen.

Table 3
Sensibility study of the specimen eigen-frequency with respect to material properties and dimensions of the specimen.

Parameters P	Ref. value	$\frac{df}{dP}$
ρ	7800 (kgm^{-3})	−0.65 Hzkg^{-1}m^3
E_{is}	204 (GPa)	52.3 HzGPa^{-1}
L_s	17.5 (mm)	−510 Hzmm^{-1}
L_c	15 (mm)	−720 Hzmm^{-1}
S_s	144 (mm^2)	−74 Hzmm^{-2}
S_c	15 (mm^2)	468 Hzmm^{-2}

3. Stress amplitude estimation

This section presents and discusses three methods used to estimate the applied stress in fatigue, namely the method of using a laser vibrometer, the method of using gauges and the method of adopting XRD.

Table 4
Frequency uncertainties (at the anti-resonance frequency of 20232Hz) due to tolerance intervals on dimensions of the specimen; all given in millimeters.

Dimensions	Tolerance Interval from criterion	Tolerance Interval from machining
L_s (mm)	±0.4 (mm)	±0.1 (mm)
L_c (mm)	±0.3 (mm)	±0.1 (mm)
S_s (mm^2)	±2.8 (mm^2)	±2.5 (mm^2)
S_c (mm^2)	±0.45 (mm^2)	±0.4 (mm^2)

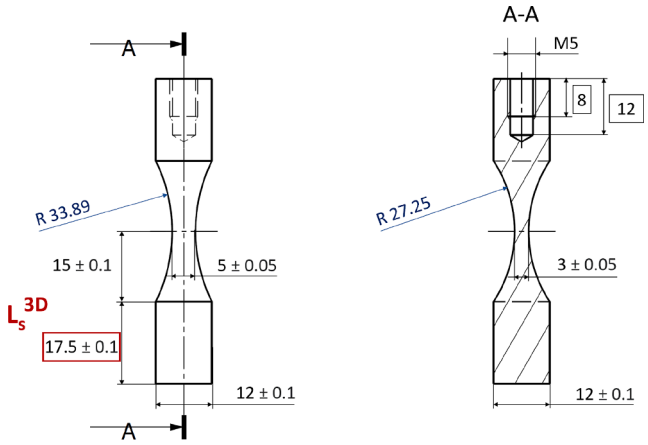

Fig. 6. Specimen geometry with optimal value of L_s. Note that the 2 opposed shaft parts of the specimen have identical dimensions. Dimensions and their tolerances are given in mm.

3.1. Method using laser vibrometer

The first method comprises two main steps. First, the displacement amplitude has to be measured on the machine without a specimen for several voltage amplitudes as shown in Section 2.1. A calibration curve like the one presented in Fig. 3 is obtained. Second, the stress amplitude in the specimen is estimated in a 3D harmonic calculation: a forced sinusoidal regime is computed with an imposed displacement amplitude of 1 μm at one end of the specimen, the other being free. The loading frequency is taken equal to 20279 Hz. A FE mesh (having an element size of 0.2 mm) finer than that employed for the harmonic calculation presented before is used as an accurate estimation of stress needs smaller elements at the center of the specimen. The stress heterogeneity along the specimen length is obtained as shown in Fig. 7. Owing to its hourglass shape, the specimen has stress heterogeneities which are measured to be between 99% and 100% of the maximal stress in a small zone of 1 mm along the longitudinal direction around the specimen center. Stress heterogeneity is also observed in the cross-section of the specimen. Fig. 8 presents a 2D map of the longitudinal stress distribution.

The specimen response is supposed to be linearly elastic, and the nominal stress amplitude is thus calculated along the x axis in the central cross-section as $\sigma_{xx} = K_s \times d_s$with K_s a factor and d_s the displacement amplitude of the end of the specimen. The mean stress factor over the central cross-section is estimated to be $K_s = 23.8$ MPa μm^{-1} for this 3D harmonic calculation. However, a non negligible stress gradient is visible throughout the cross-section. As the stress is measured at the surface of the specimen, when using the methods adopting strain gauges

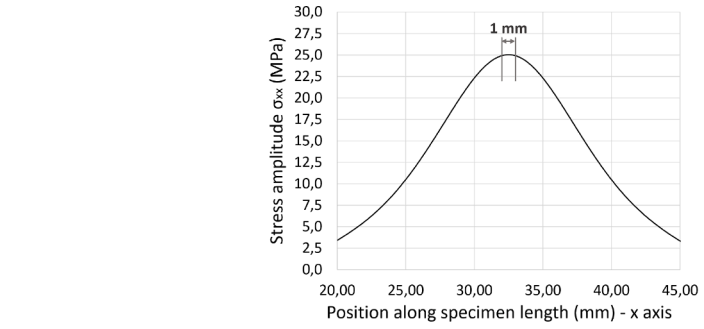

(a)

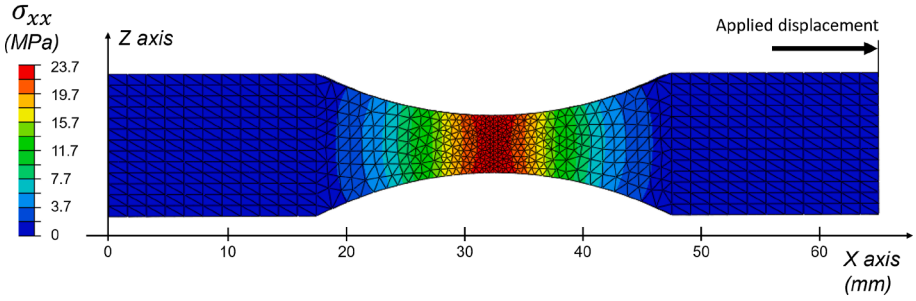

(b)

Fig. 7. a) Longitudinal stress amplitude along the specimen central axis and b) longitudinal stress amplitude field (applied displacement amplitude $1\mu m$; loading frequency 20279Hz).

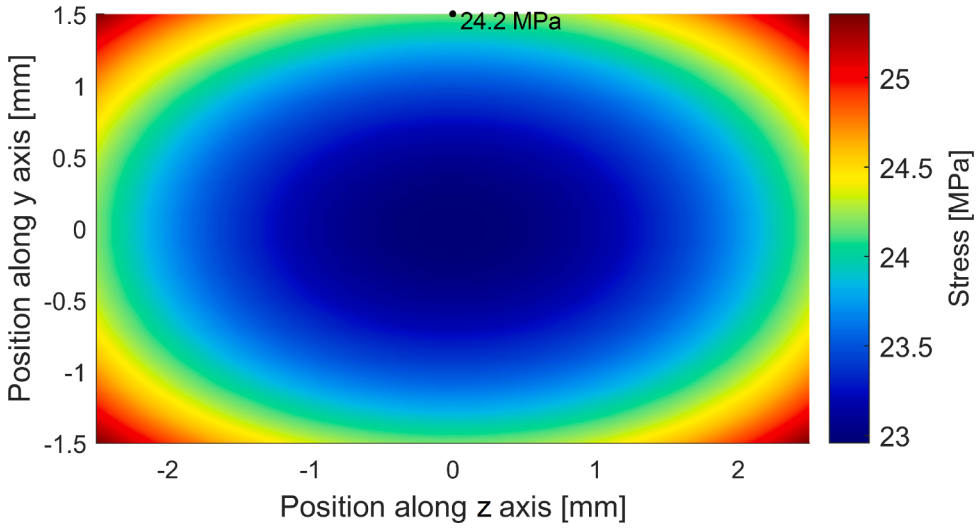

Fig. 8. Longitudinal stress amplitude distribution within the specimen cross-section, in the center of the specimen for an applied displacement of 1μm at a frequency of 20279Hz.

and XRD, the stress factor $K_s = 24.2$ MPa μm^{-1} is used in the following.

Two main sources of systematic errors have been identified. The uncertainties in material parameters (see Table 2) result in an error of 2% in the stress in the 3D harmonic calculations. Additionally, the construction of the calibration curve introduces a discrepancy of around 1.2% (see Section 1) on the estimation of the displacement amplitude for a given stress amplitude. The systematic error made in the estimation of stress on the cross-section of the specimen using the laser vibrometer is approximately 3.2% because the stress estimation is a linear multiplication of the displacement and stress factor. Moreover, the experimental laser measurements introduce a 1% random error in the whole calculation (see Section 2.1), which is negligible compared to the estimated systematic error [5].

3.2. *Method using strain gauges*

Strain gauges are widely used to measure the total longitudinal strain in a specimen loaded at 20 kHz. Two gauges (*KYOWA KFG-1 N-120-C1-*

[5] Note that possible additional errors due to visco-elastic (instead of elastic) response of the material can hardly be estimated.

11) are glued facing each other on opposite surfaces of the central cross-section. The useful area of a gauge has dimensions of around 1 mm × 0.64 mm and is oriented with its length along the specimen length. These gauges can measure strain as low as 10^{-6}. Gauges are set in a full bridge circuit. A KYOWA (CDV-700A) signal conditioner is used to power the bridge and to amplify the output voltage. Two additional gauges (which are thermally compensated as should be for a full compensation of any room change in temperature) are glued on a second (dummy) specimen of the same material.

Strain gauges can measure the total strain in less than a micro-second for the reconstruction of one cycle described by 50 points. From strain gauges measurements during a fatigue test conducted at 20 kHz, Fig. 9 presents the reconstructed evolution of strain with respect to time. In fact, each point on the curve is the mean of strain gauges values obtained for 200000 successive fatigue cycles.

Assuming a purely elastic material response we estimate the longitudinal stress at the center of the specimen as: $\sigma = E_{is} \times \varepsilon_e$. The random error (i.e., the standard deviation of the 200000 values) is approximately 2% and tends to decrease with increasing the number of gauge acquisitions. The gauge method has two sources of systematic errors. First, the measurement of the elastic modulus introduces a 2% error. Second, uncertainty emerging from the use of the strain gauge amplifier during calibration with a shunt resistance, is approximately 1% of the measured strain value. The total systematic error is therefore around 3%. The random error is kept smaller than the systematic error.

3.3. Method adopting XRD

A cyclic deformation of the specimen leads at the micro-scale (grain scale) to an elastic deformation that is heterogeneous owing to the anisotropy of the elastic grain behavior, for example see [28–30]. This micro-scale elastic deformation, when measured along the normal of the specific (hkl) lattice plane of the grains of the specimen, is usually referred to as lattice strain in the literature. Because the set of crystallites under diffraction conditions (i.e. "the diffraction volume") is only part of the whole specimen, scale transition models, which bridge the grain deformation with the macroscopic strain, are required to invert the diffraction data. Here, a micro–macro Self-Consistent (SC) model [31,32] was used to estimate the X-ray elastic constants (XECs) [33,34] for the studied material; these XECs relate the lattice strain with the applied macroscopic strain according to anisotropic elastic behavior. The SC model considers the volume fraction of ferrite and cementite in the steel as well as the crystallographic texture and average grain shape. Once the XECs are estimated, there is a linear relation between the lattice strain of the diffracting crystallites for the *hkl* reflection and the macroscopic longitudinal stress in the specimen. During fatigue loading, the cyclic shift of the *hkl* diffraction peak is representative of the evolution of the average inter-reticular spacing among the *hkl* grains under the diffraction condition; that is, the average elastic strain of this set of grains. According to Bragg's law (2), and for polycrystalline material, the x-rays diffracted by crystallographic planes having Miller indexes *hkl* and inter-reticular spacing d_{hkl} are located across a cone aligned with the incident beam and a half-apex of 2θ (see Fig. 11a):

$$\lambda = 2d_{hkl}\sin\theta. \tag{4}$$

The cone is intercepted with a 2D detector which only sees a ring. This ring, once integrated along its length, is represented as a 1D *hkl* diffraction peak.

The in situ time-resolved XRD method applied to ultrasonic fatigue tests is a recently developed technique detailed in [18,19]. Its principle is the estimation of the applied stress (through the measurement of the lattice strain) from the measured $\Delta 2\theta$ shift of the diffraction peak position on the 2D detector. Several prerequisites must be fulfilled to estimate the applied stress from XRD data. First, the XRD images obtained on the detector must have counting statistics sufficient to reduce the photon noise. A stroboscopic method has been developed to improve the counting statistics (Fig. 10). Within a single detector opening (which lasts 1 µs), few photons are captured by the detector, and this leads to an image with too much photon noise. To reduce this noise, we need to capture more photons by accumulating many detector integration times for a given stress level within the loading cycles. To generate such a stroboscopic acquisition mode, the gauge signal is used to trigger the opening of the detector and thus the capture of one image. This process is repeated over many thousands of times (e.g. 200000 times in this study) to obtain sufficiently low image noise. To describe one period of oscillation with enough points as for the strain gauge method (around 50 points), the temporal resolution of the method is set at 1 µs. This corresponds to the opening duration of the detector used to capture the diffracted x-rays photons. After each image acquisition, an additional small delay is applied to the trigger so that the next detector image is captured at a different stress level within the sinusoidal loading. The setup requires an electronic system that synchronizes the short electronic opening of the detector with the cyclic deformation applied by the piezo-electric machine, see [18] for further details.

The above mentioned stroboscopic method, which requires very short opening durations for the detector shutter, only works when using an extremely brilliant X-ray source and a detector equipped with an electronic shutter. These prerequisites are met at the DiffAbs beamline of

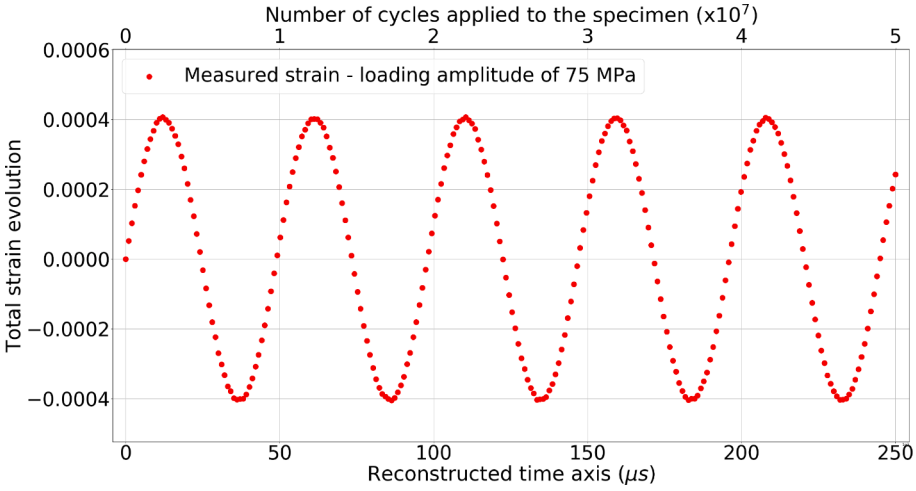

Fig. 9. Total strain evolution for a fatigue test at 75MPa during 5 cycles. The top x-axis represents the number of cycles as seen by the specimen during the measurements.

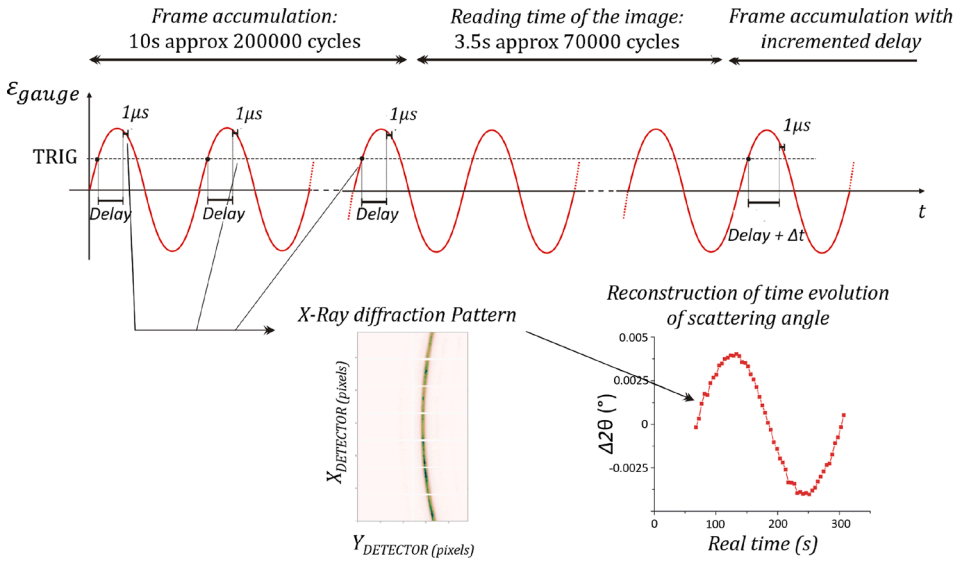

Fig. 10. Stroboscopic principle for data acquisition - Case of a reconstructed 2θ diffraction peak position for a loading amplitude of 190MPa (adapted from Ors et al. [18]).

the SOLEIL Synchrotron in France. The ultrasonic fatigue machine, with the specimen mounted on it, is placed horizontally in the diffractometer. The specimen center is aligned with the rotation center of a 4-circles goniometer and with an incident monochromatic X-ray beam coming from the synchrotron source (A wavelength $\lambda = 0.775$ nm is used here). Part of the diffraction cone is intercepted by a 2D planar hybrid pixel detector (an XPAD S140 with a pixel size of 130×130 µm^2 in our case) [35]. To reduce geometrical aberration, diffracting surfaces with a small curvature of radius are generally preferred to cylindrical specimens, and a rectangular cross-section is thus considered in this study. The specimen surface is then tilted by $10° - 20°$ with respect to the incident beam to provide a reflection configuration. Fig. 11 shows the experimental setup. When the fatigue machine is started, the applied stress creates elastic strain in the specimen leading to slight periodic changes in d_{hkl}. The aperture 2θ of the diffraction cone is thus expected to be modified accordingly at the same frequency. With a cross-section of the incoming beam of typically 200×300 µm and a penetration depth of ~ 40 µm at the used wavelength, a large number of grains are measured simultaneously [6]. As an illustrative example, with the used setup, the 110 diffraction peak of the C70 steel studied here has a Full-Width at Half Maximum of typically 0.1° (corresponding to ~ 9 detector pixels), the signal-to-noise ratio is in excess of 90 and the maximum intensity is in the $10^5 - 10^6$ counts range. The fitting of diffraction peaks with an asymmetrical Pearson VII distribution leads to errors on the order of 4.10^{-4} degrees in the 2θ angle. At the 2θ angle observed here (22°), this corresponds to random error of up to 8% in the estimation of elastic strain.

The XEC of the ferrite α phase, in the case of the peak 110 is estimated as -1.32×10^{-6} MPa^{-1}. The uncertainty in the estimation of the X-ray elastic constants has to be considered because it is linearly related to the macroscopic stress amplitude. Such an uncertainty is difficult to assess because an XEC depends on both the single crystal elastic constants and the specimen microstructure (e.g. the crystallographic texture, grain shape, and grain arrangement) which can be characterized experimentally only partly, and on a volume supposed to be sufficiently large to be statistically representative of the material but again within a certain degree of accuracy. The elastic SC model itself, as a scale transition model, is found to provide results that are close to those of reference full-field computational homogenization methods, with the relative discrepancies being in the 10^{-3} range [36,29]. The accuracy of the XEC is thus essentially limited by the lack of precise knowledge of the single crystal elastic constant and of the microstructure. The precise determination of the anisotropic stiffness at the grain scale in a given polycrystalline aggregate is not an easy task because we need to probe single grains individually [37], such as through nano-indentation, or by inversing XRD data as in [38]. Meanwhile, to the best of our knowledge, the estimation of the effect of microstructure on the XEC has not been thoroughly investigated in the literature. Notably, however, small microstructure effects were reported in [30] for architectured two-phase materials, with the difference in results between the used models and X-ray and neutron diffraction data being better than 10%. A similar conclusion was drawn by [39], with the discrepancy between the XECs estimated by the SC scheme and those computed using a full-field FE model, in which an (unrealistic) microstructure with cubic grains was considered, being mostly better than 10%. Additionally, the difference in the XECs of the (110) plane in ferrite estimated using Reuss and Voigt bounds, which provide rigorous lower and upper bounds for the elastic stiffness whatever the specimen microstructure, is 8%. One therefore expects that microstructure effects may be smaller than this difference. The accuracy of estimating stress using the X-ray method must account for the discrepancy sources cited above and the stress is therefore assessed estimated with an overestimated systematic error of 10%. Therefore, the random error determined above is negligible compared to the systematic error.

4. Results and Discussion

4.1. Comparison of Methods

During the synchrotron experiments, the specimen was loaded at ambient temperature and continuously cooled by a compressed cold air flow. Stress amplitudes from 75 MPa to 258 MPa were applied. As discussed above, the stress estimation requires to assume that the specimen response is purely elastic in the laser vibrometer and strain gauge methods whereas this assumption is not necessary when using the XRD method. In the method using a laser vibrometer, for comparion with XRD and gauges methods, the K_s factor was taken at the surface of the modeled specimen such that $K_s = 24.2$ MPa µm^{-1}, as already discussed in Section 3.1. As the method using XRD estimates stresses from elastic

[6] As the specimen surface is tilted by a few degrees from the beam direction, the size of the illuminated surface on the material is approximately 1000×300 µm^2

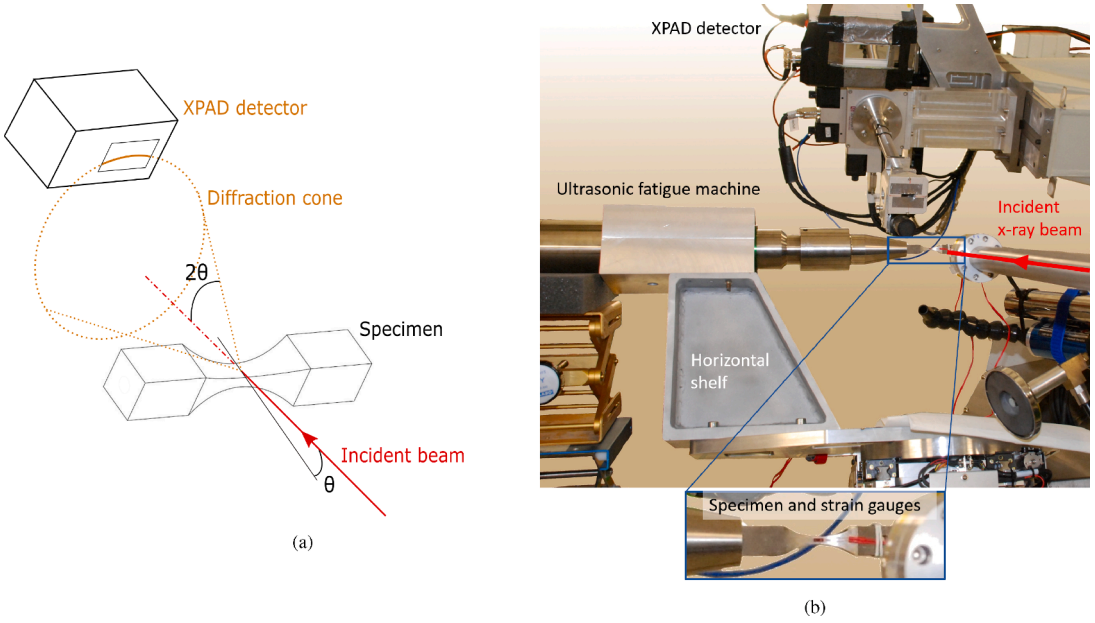

Fig. 11. Experimental setup of the XRD method - a) schematic view b) picture of the setup installed at DiffAbs beamline at synchrotron SOLEIL, in France.

strain measurements, the consistent results between the three methods prove that assuming an elastic response in the studied stress amplitude range is accurate enough. The studied stress amplitude range corresponds to two third of the yield stress of the material and it is below the fatigue strength at 10^9 cycles. It covers most of the VHCF loading domain.

Results obtained using the three methods are plotted in Fig. 12. In this figure, the stress amplitude increases linearly with increasing displacement amplitude (which was measured at the free end of the horn). The values show good agreement among the three methods. Systematic measurement errors for each method, which were discussed earlier, are plotted as error-bars in Fig. 12.

The high number of values used in obtaining average gauge and laser vibrometer measurements and the high number of accumulated XRD frames reduce the effect of random error. These errors were not considered in this comparison.

4.2. Stress distribution along the specimen length

One advantage of the XRD method is that the measurement is carried out in a small region of the surface of the specimen. The stress can therefore be estimated along the specimen length when the beam is positioned to probe different positions. Fig. 13 compares the results obtained with the method adopting XRD with the results obtained with the methods using the laser vibrometer and strain gauges.

Notably, the stress heterogeneity measured with the XRD method effectively matches the 3D simulation with a similar stress distribution along the specimen length. The tails of the distribution obtained using the XRD method are a little tighter than those estimated using the FEM but their tendancies are the same. The XRD method obtains a strong vertical dispersion of about ±10 MPa in the central zone, which is about 8% of the XRD values. This dispersion is in good agreement with the random errors estimated in Section 3.3. This random error might be alleviated by a longer exposure time or finer spatial and temporal resolution. Additionally, all XRD measurements conducted apart from that at the specimen center have a slightly different experimental configuration with a different sample surface orientation with respect to the incident X-ray beam and detector. These slight changes in configuration might be a source of discrepancy with FEM modeling for data away from the specimen center shown in Fig. 13. The three methods give similar results when it comes to estimating the stress amplitude on the surface at the center of the specimen but the methods provide different

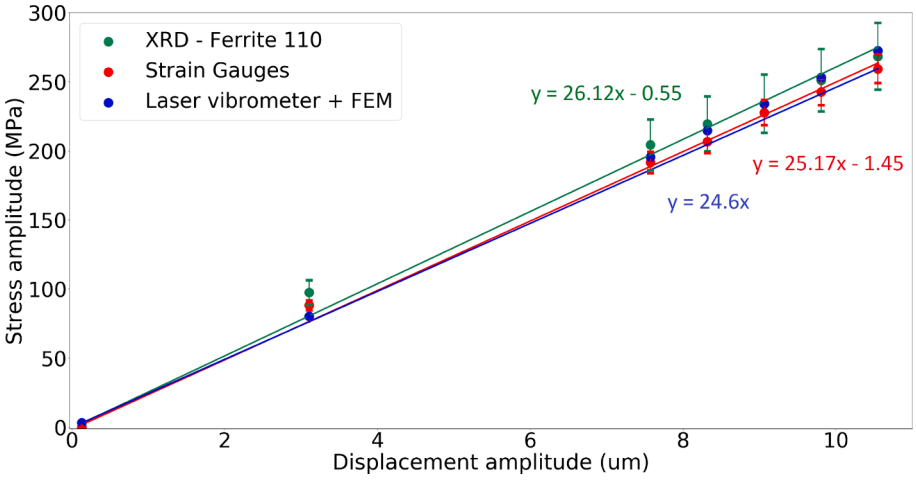

Fig. 12. Stress amplitude plotted with respect to displacement amplitude applied to the specimen.

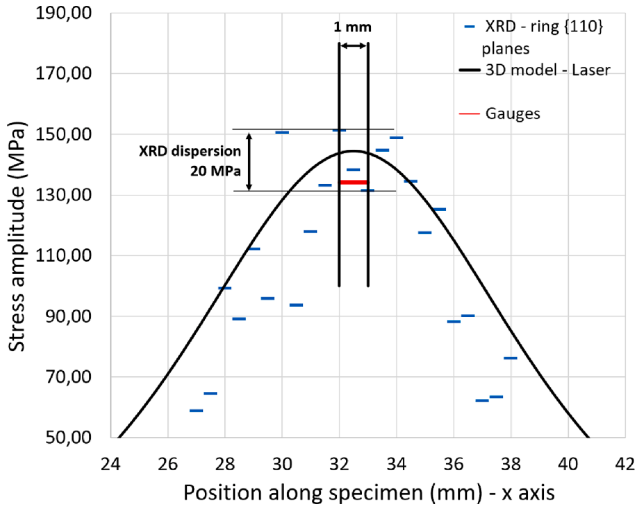

Fig. 13. Stress heterogenities assessment along the specimen length. The three methods are compared (gauges in red, XRD in blue and Laser as the black straight line). The length of horizontal markers corresponds to the spatial resolution of each method.

possibilities in estimating the spatial stress distribution. The strain gauge method is a local estimation across the gauge surface whereas the numerical calculation of the laser vibrometer method gives information on the spatial distribution of stress in the specimen. Meanwhile, the XRD method allows us to estimate experimentally the stress distribution on a large specimen surface without relying on a harmonic calculation of the specimen response.

5. Summary and Conclusion

This paper presented and compared three methods of estimating the stress amplitude. The limits of these methods were investigated and conclusions on their capability and reliability in estimating the stress amplitude during a fatigue test conducted at 20 kHz were drawn. Additionally, the complete methodology of conducting a fatigue test at tens of kilohertz, from the detailed functioning of the ultrasonic fatigue machine to the specimen design, was presented. Methods of assessing stress amplitudes were presented to complete the description of the experimental process.

The comparison of the three methods is summarized as follows:

- The uncertainty in the isentropic modulus causes the largest deviation between the optimum operating frequency of the ultrasonic machine and the real test frequency.
- In the case of a well-designed specimen, the deviations in dimensions owing to the manufacturing process lead to deviations in frequency lower than that induced by the uncertainty in the isentropic modulus.
- The frequency drift results in a deviation of the displacement amplitude imposed on the specimen of 2% compared to that prescribed to the machine.
- The method using strain gauges is the easiest to adopt because it only requires strain gauges to be glued on the surface of the specimen. It provides an accurate estimate of the longitudinal stress amplitude with an accuracy of 3%. The method is based on the hypothesis that the specimen response remains purely elastic during the whole test duration. However, it provides no information about strain heterogeneity along the specimen length.
- The method using a laser vibrometer cannot provide useful results without being coupled with a 3D FEM harmonic computation. The method then gives a precise and accurate estimation of the stress amplitude (with an uncertainty of 3.2%) for every part of the specimen but, like the method using strain gauges, and is based on the hypothesis of a purely elastic specimen response during loading. Furthermore, the calibration process is reliable only for the specimens for which the calibration was checked (see Section 2.4).
- In the case of the time-resolved XRD method, the stress amplitude accuracy essentially depends on the estimation of the XECs. Limitations mostly relate to the knowledge of the single crystal elastic constant and material microstructure. The used X-ray setup must also be calibrated to high accuracy. In addition to its unique capacity of measuring the stress at different scales (e.g. using a different beam size) and spatial positions by scanning the whole specimen surface with the incoming beam, an important advantage of the method is that it does not rely on a hypothesis of the mechanical response of the specimen. It thus allows the stress to be followed during the loading cycles. Even so, this method requires a micro–macro model and a synchrotron facility that provides a high X-ray flux, a well collimated X-ray beam and a detector for time-resolved analysis. As observed in this study, the method adopting XRD introduces a larger systematic error compared to the two other methods.

The comparison of the three methods reveals that considering a purely elastic response of the specimen is a valid approximation for the estimation of the applied stress, up to amplitudes close to the fatigue strength. It was seen that the XRD method that does not rely on this assumption provided results that are in good agreement with those of the two methods that are based on this assumption.

Declaration of Competing Interest

The authors declare that they have no known competing financial interests or personal relationships that could have appeared to influence the work reported in this paper.

Acknowledgements

This study was conducted in the framework of the european research project H2020 FastMat (fast determination of fatigue properties of materials beyond one billion cycles) funding by the European Research Council (ERC) (grant agreement No 725142). Synchrotron SOLEIL is acknowledged for granting beamtime for XRD experiments under project no: 2018–1123. P. Joly is acknowledged for provding technical support and Edanz (www.edanz.com/ac) for editing a draft of this manuscript.

References

[1] Mayer H, Haydn W, Schuller R, Issler S, Furtner B, Bacher-Höchst M. Very high cycle fatigue properties of bainitic high carbon–chromium steel. Int. J. Fatigue 2009;31:242–9. https://doi.org/10.1016/j.ijfatigue.2008.09.001. URL: http://www.sciencedirect.com/science/article/pii/S014211230800217X.

[2] S. Stanzl-Tschegg, Ultrasonic fatigue, in: K.J. Buschow, R.W. Cahn, M.C. Flemings, B. Ilschner, E.J. Kramer, S. Mahajan, P. Veyssière (Eds.), Encyclopedia of Materials: Science and Technology, Elsevier, Oxford, 2001, pp. 9444–9449. URL: http://www.sciencedirect.com/science/article/pii/B0080431526017071. doi: 10.1016/B0-08-043152-6/01707-1.

[3] Marti N, Favier V, Saintier N, Gregori F. Investigating Fatigue Frequency Effects on Single Phase Ductile Materials. Procedia Eng. 2015;133. https://doi.org/10.1016/j.proeng.2015.12.675. URL: https://linkinghub.elsevier.com/retrieve/pii/S1877705815045944.

[4] Mason WP. Physical Acoustics and the Properties of Solids. Princeton, NJ: van Nostrand; 1958.

[5] C. Fischer, R. Wagener, A. Friedmann, C. Axt, T. Melz, Piezoelectric driven testing facilities to research the very high cycle fatigue regime, Berger C, Christ H-J, editors, 2011, pp. 427–432.

[6] M. Schmidt, M.T. Friedman A, Drögemüller T, Hybride prüftechnik zur dynamischen charakterisierung von elastomerbauteilen, volume Werkstoffprüfung, Konstruktion, Werkstoffentwicklung und Schadensanalyse, 2010, pp. 161–166.

[7] Marines I, Bathias C, Bin X. An understanding of very high cycle fatigue of metals. Int. J. Fatigue 2003;25:1101–7. https://doi.org/10.1016/S0142-1123(03)00147-6. URL: https://linkinghub.elsevier.com/retrieve/pii/S0142112303001476.

[8] Wu T, Ni J, Bathias C. An Automatic Ultrasonic Fatigue Testing System for Studying Low Crack Growth at Room and High Temperatures. In: Amzallag C,

editor. Automation in Fatigue and Fracture: Testing and Analysis. West Conshohocken, PA: ASTM International; 1994. p. 598–607. https://doi.org/10.1520/STP13973S.
[9] Bathias C. Piezoelectric fatigue testing machines and devices. Int. J. Fatigue 2006; 28:1438–45. https://doi.org/10.1016/j.ijfatigue.2005.09.020. URL: https://linkinghub.elsevier.com/retrieve/pii/S0142112306001095.
[10] Stanzl-Tschegg S. Very high cycle fatigue measuring techniques. Int. J. Fatigue 2014;60:2–17. https://doi.org/10.1016/j.ijfatigue.2012.11.016. URL: https://linkinghub.elsevier.com/retrieve/pii/S0142112312003581.
[11] Sun C, Song Q, Hu Y, Wei Y. Effects of intermittent loading on fatigue life of a high strength steel in very high cycle fatigue regime. Int. J. Fatigue 2018;117:9–12. https://doi.org/10.1016/j.ijfatigue.2018.07.033. URL: http://www.sciencedirect.com/science/article/pii/S0142112318303190.
[12] Furuya Y, Matsuoka S, Abe T, Yamaguchi K. Gigacycle fatigue properties for high-strength low-alloy steel at 100 Hz, 600 Hz, and 20 kHz. Scr. Mater. 2002;46: 157–62. https://doi.org/10.1016/S1359-6462(01)01213-1. URL: https://linkinghub.elsevier.com/retrieve/pii/S1359646201012131.
[13] Crossland B. Effect of a large hydrostatic pressure on the torsional fatigue strength of an alloy steel 1956:138–49.
[14] Dang-Van K, Griveau B, Message O. On a new multiaxial fatigue limit criterion: theory and application, biaxial and multiaxial fatigue. EGF Publication 1982;3: 479–96.
[15] Radmanovic MD, Mancic DD. Design and modeling of the power ultrasonic transducers, MP Interconsulting. Le Locle 2004;OCLC:932559511.
[16] Messager A, Junet A, Palin-Luc T, Buffiere J-Y, Saintier N, Ranc N, El May M, Gaillard Y, King A, Bonnin A, Nadot Y. In situ synchrotron ultrasonic fatigue testing device for 3d characterisation of internal crack initiation and growth. Fatigue Fract. Eng. Mater. Struct. 2019;43:558–67. https://doi.org/10.1111/ffe.13140. URL: https://onlinelibrary.wiley.com/doi/abs/10.1111/ffe.13140.
[17] Brugger C, Palin-Luc T, Osmond P, Blanc M. A new ultrasonic fatigue testing device for biaxial bending in the gigacycle regime. Int. J. Fatigue 2017;100:619–26. https://doi.org/10.1016/j.ijfatigue.2016.12.039. URL: https://linkinghub.elsevier.com/retrieve/pii/S0142112316304558.
[18] Ors T, Ranc N, Pelerin M, Michel V, Favier V, Castelnau O, Mocuta C, Thiaudière D. Microsecond time-resolved x-ray diffraction for the investigation of fatigue behavior during ultrasonic fatigue loading. J. Synchrotron Radiat. 2019;26: 1660–70. https://doi.org/10.1107/S1600577519008518.
[19] Fitzka M, Rennhofer H, Catoor D, Reiterer M, Lichtenegger H, Checchia S, di Michiel M, Irrasch D, Gruenewald TA, Mayer H. High Speed In Situ Synchrotron Observation of Cyclic Deformation and Phase Transformation of Superelastic Nitinol at Ultrasonic Frequency. Exp Mech 2020;60:317–28. https://doi.org/10.1007/s11340-019-00562-8. URL: http://link.springer.com/10.1007/s11340-019-00562-8.
[20] Liu L, Husseini N, Torbet C, Lee W-K, Clarke R, Jones J, et al. In situ synchrotron X-ray imaging of high-cycle fatigue crack propagation in single-crystal nickel-base alloys. Acta Mater. 2011;59:5103–15. https://doi.org/10.1016/j.actamat.2011.04.042. URL: https://linkinghub.elsevier.com/retrieve/pii/S1359645411002989.
[21] Wagner D, Cavalieri F, Bathias C, Ranc N. Ultrasonic fatigue tests at high temperature on an austenitic steel. Propuls. Power Res. 2012;1:29–35. https://doi.org/10.1016/j.jppr.2012.10.008. URL: https://linkinghub.elsevier.com/retrieve/pii/S2212540X12000090.
[22] Puškár A. Ultrasonic fatigue testing equipment and new procedures for complex material evaluation. Ultrasonics 1993;31:61–7. https://doi.org/10.1016/0041-624X(93)90034-W. URL: https://linkinghub.elsevier.com/retrieve/pii/0041624X9390034W.
[23] Mayer H. Fatigue crack growth and threshold measurements at very high frequencies. Int. Mater. Rev. 1999;44:1–34. https://doi.org/10.1179/imr.1999.44.1.1.
[24] Peng W, Zhang Y, Qiu B, Xue H. A Brief Review of the Application and Problems in Ultrasonic Fatigue Testing. AASRI Procedia 2012;2:127–33. https://doi.org/10.1016/j.aasri.2012.09.024. URL: https://linkinghub.elsevier.com/retrieve/pii/S2212671612001230.
[25] Bruchhausen M, Hähner P, Fischer B, Cornu D. Device for carrying out environmental very high cycle fatigue tests with ultrasonic excitation in asymmetric push–pull mode. Int. J. Fatigue 2013;52:11–9. https://doi.org/10.1016/j.ijfatigue.2013.02.010. URL: https://linkinghub.elsevier.com/retrieve/pii/S0142112313000492.
[26] H. Yahiaoui, Effet de l'espacement interlamellaire sur le comportement sous chargements monotone et cyclique de l'acier perlitique C70., Ph.D. thesis, ENSAM Paris, 2013. URL: http://www.theses.fr/2013ENAM0025.
[27] Blanche A, Chrysochoos A, Ranc N, Favier V. Dissipation Assessments During Dynamic Very High Cycle Fatigue Tests. Exp. Mech. 2015;55:699–709. https://doi.org/10.1007/s11340-014-9857-3. URL: http://link.springer.com/10.1007/s11340-014-9857-3.
[28] Brenner R, Lebensohn R, Castelnau O. Elastic anisotropy and yield surface estimates of polycrystals. Int. J. Solids Struct. 2009;46:3018–26. https://doi.org/10.1016/j.ijsolstr.2009.04.001. URL: http://www.sciencedirect.com/science/article/pii/S0020768309001632.
[29] R. Lebensohn, P. Castañeda, R. Brenner, O. Castelnau, Computational Methods for Microstructure-Property Relationships, ghosh, somnath and dimiduk, dennis ed., Springer, 2011, pp. 393–441.
[30] Gu T, Castelnau O, Forest S, Herve-Luanco E, Lecouturier F, Proudhon H, Thilly L. Multiscale modeling of the elastic behavior of architectured and nanostructured cu-nb composite wires. Int. J. Solids Struct. 2017;121:148–62.
[31] Hershey AV. The elasticity of an isotropic aggregate of anisotropic cubic crystals. J. of Appl. Mech. 1954;21:236–40.
[32] Kröner E. Self-consistent scheme and graded disorder in polycrystal elasticity. J. Phys. F: Metal Phys. 1978;8:2261–7.
[33] Faurie D, Castelnau O, Brenner R, Renault P-O, Le Bourhis E, Goudeau P. In situ diffraction strain analysis of elastically deformed polycrystalline thin films, and micromechanical interpretation. J. Appl. Cryst. 2009;42:1073–84. https://doi.org/10.1107/S0021889809037376.
[34] Vermeulen AC, Kube CM, Norberg N. Implementation of the self-consistent kröner–eshelby model for the calculation of x-ray elastic constants for any crystal symmetry. Powder Diffr. 2019;34:103–9. https://doi.org/10.1017/S088571561900037X.
[35] Landois P, Djaziri S, Renault P-O, Le Bourhis E, Goudeau P, Pinault M, Mayne-L'Hermite M, Bacroix B, Faurie D, Castelnau O, Launois P, Rouzière S. Synchrotron x-ray diffraction experiments with a prototype hybrid-pixel detector. J. App. Cryst. 2012;45:38–47.
[36] Lebensohn R, Castelnau O, Brenner R, Gilormini P. Study of the antiplane deformation of linear 2-d polycrystals with different microstructures. Int. J. of Solids Struct. 2005;42:5441–59. https://doi.org/10.1016/j.ijsolstr.2005.02.051. URL: http://www.sciencedirect.com/science/article/pii/S0020768305000958.
[37] Plancher E, Favier V, Maurice C, Bosso E, Rupin N, Stodolna J, Loisnard D, Marijon J-B, Petit J, Micha J-S, Robach O, Castelnau O, et al. Direct measurement of local constitutive relations, at the micrometre scale, in bulk metallic alloys. J. Appl. Crystallogr. 2017;50:940–8. https://doi.org/10.1107/S1600576717006185. URL: https://hal.archives-ouvertes.fr/hal-01663617.
[38] R. Raj Purohit Purushottam, T. Richeton, S. Berbenni, L. Germain, N. Gey, T. Connolley, O. Castelnau, Estimating single-crystal elastic constants of polycrystalline β-metastable titanium alloy: A bayesian inference analysis based on high energy x-ray diffraction and micromechanical modeling, Acta Mater. (submitted).
[39] Zhang Y, Chen W, McDowell DL, Wang YM, Zhu T. Lattice strains and diffraction elastic constants of cubic polycrystals. J. Mech. Phys. Solids. 2020;138:103899. https://doi.org/10.1016/j.jmps.2020.103899. URL: http://www.sciencedirect.com/science/article/pii/S0022509620301356.